

MODELING, CONTROL, AND TESTING OF AC PM AND RELUCTANCE ELECTRIC MACHINES FOR RENEWABLE ENERGIES AND AUTOMOTIVE APPLICATIONS

PhD Thessis – Summary

for obtaining the Scientific Title of PhD in Engineering from Politehnica University Timişoara in the Field of Electrical Engineering

author ing. Liviu-Dănuț VITAN

scientific supervisor: Prof.dr.ing. Nicolae MUNTEAN month 03, year 2025

This thesis presents comprehensive characterizations and new control strategies for PM and reluctance electric machines highlighted in renewable and automotive applications. Four control strategies are proposed and analyzed: a sensorless method for a synchronous reluctance machine with flux barriers used as a generator (SynRG), and three encoder-based strategies dedicated to an axially laminated anisotropic rotor reluctance synchronous machine (ALA Rotor RSM) and to an interior permanent magnet synchronous machine (IPMSM), both used as traction motors. The ALA Rotor RSM and IPMSM are newly designed and manufactured prototypes, investigated here in an effort to provide improved electrical machines with lower costs and better performances over a wide speed range.

A stability analysis is performed for the sensorless control method, which aims to provide the PI controller coefficients for which the observer is stable and how the machine parameter uncertainties influence it.

The proposed control method for the ALA Rotor RSM is based on a first-order offline computed function using the measured dq-axis inductances with cross-coupling effect prior to commissioning. The method aims to drive the ALA Rotor RSM closely to its maximum efficiency, even when it is highly saturated. A second proposed control strategy based on a look-up table function using the measured dq-axis current pairs that yield the highest efficiency for the ALA Rotor RSM and its drive inverter is used to validate the effectiveness of the first method.

The final part of the thesis presents a proposed concept for a fully electric city minibus intended for public transportation using supercapacitors (SC) as a storage element, a single IPMSM with Bonded-NdFeB Spoke PMs for traction, and a hybrid bidirectional DC-DC converter for power transfer between the SC and IPMSM drive inverter. Two cases are investigated: a full-scale model (1:1) for which simulation results in real traffic operating conditions are provided and a lab-scale model (1:20) where both simulation and experimental results are presented. The proposed control strategy for the IPMSM is also tested in relation to the other components of the minibus power system, such as the HBDC and the SC.



Chapter 1 presents an introduction to the field and analyses the EU Directives, Regulations, and targets concerning electric motor efficiency and the enhancement of energy production from renewable sources. It also emphasizes industry trends focused on developing new, high-efficiency motors.

Furthermore, a survey of the main sensorless control strategies for synchronous reluctance machines (Fig. 1) is presented, and a literature review is conducted on methods for determining parameters of electrical machines and control strategies with encoder for the ALA Rotor RSM and IMPMSM. Also, it explores the power system of fully electric vehicles, mainly of those that use supercapacitors as a storage element.

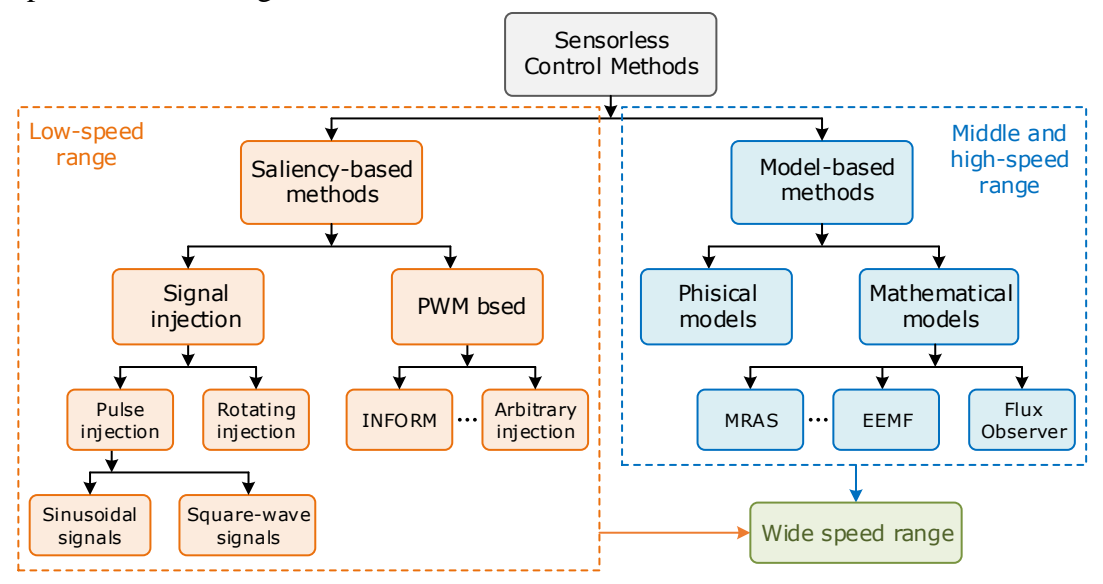


Fig. 1 The main sensorless control methods for SynRMs [1], [2]

The development of renewable energy sources, electric vehicles (EVs), and growing demand for energy efficiency have pushed the evolution of traditional AC power distribution to hybrid AC/DC grids. The benefits of integrating DC infrastructure along with AC distribution are highlighted by the many renewable energy sources that naturally provide DC power, battery storage systems, and the rise of EVs with DC charging systems. Additionally, the AC/DC grids with the EVs can create a strong synergy by sharing power bidirectionally, known as vehicle-togrid applications, which opens opportunities for grid stabilization and energy storage. In this context, a possible residential AC/DC grid named nanogrid, which includes a wind turbine and photovoltaic panels as energy sources, a battery storage system, bidirectional power flow, and DC-fed appliances, is presented, including the interface with the EVs [3], [4].

Chapter 2 presents a different proposed sensorless control strategy for a low-speed Synchronous Reluctance Machine (SynRM) operating as a generator [5]. An observer is implemented to determine the rotor angular position using the SynRM model and the error between the measured and estimated q-axis currents. The effectiveness of the rotor position estimation is evaluated under various operating conditions while considering the uncertainty of the SynRM parameters. A stability analysis is performed through model linearization using small-signal deviations to investigate the stability of the estimator model, which also defines the appropriate range for the proportional-integral controller (PI) coefficients. Simulations were conducted to



verify the control methodology and to compare the angular position determined by the estimator with that obtained from the SynRM model. Experimental tests were performed on a six pole pairs, 200rpm, 1.8kW SynRM, to verify and substantiate the theoretical assumptions.

The proposed structure for the Synchronous Reluctance Generator (SynRG) is presented in Fig. 2. This includes a Prime Mover, which drives the SynRG, having as input a speed reference. The Prime Mover can be a wind turbine, hydro turbine, steam turbine, diesel engine, or any prime mover capable of producing mechanical angular speed and torque. Of course, to reduce pollution, the Prime Mover should utilize a renewable energy source. An inverter drives the SynRG, which has its DC Link connected to a DC grid to deliver the energy harvested from the SynRG. During the commissioning procedure or when the Prime Mover is not operating, the inverter draws power from the DC grid to supply its internal circuits. The control strategy is implemented in the dq rotor reference frame. The power reference for the SynRG is obtained by prescribing the d-axis current (i_d^*) and the q-axis current (i_q^*) . These are compared with the measured dq-axis current $(i_{d\hat{\theta}_{ar}})$ and $i_{q\widehat{\theta}_{er}}$) provided by the observer block based on the estimated angular position $(\widehat{\theta}_{er})$. The current errors are processed through the PI controllers to obtain the reference dq-axis reference voltages (V_d^*, V_d^*) . The phase references voltages $(V_{a,b,c}^*)$ for the inverter's PWM unit are obtained by applying inverse Park and Clarke transformations to the dq-axis voltage references. The estimated angular position $(\hat{\theta}_{er})$ required for the coordinate transformation and speed estimation, is provided by the observer based on the measured phase currents (iabc) of the SynRG and the inverter's DC-Link voltage (V_{dc}) . The V_{dc} is used along with phase reference voltages to compute the estimated supplied phase voltages (V_{abc}) .

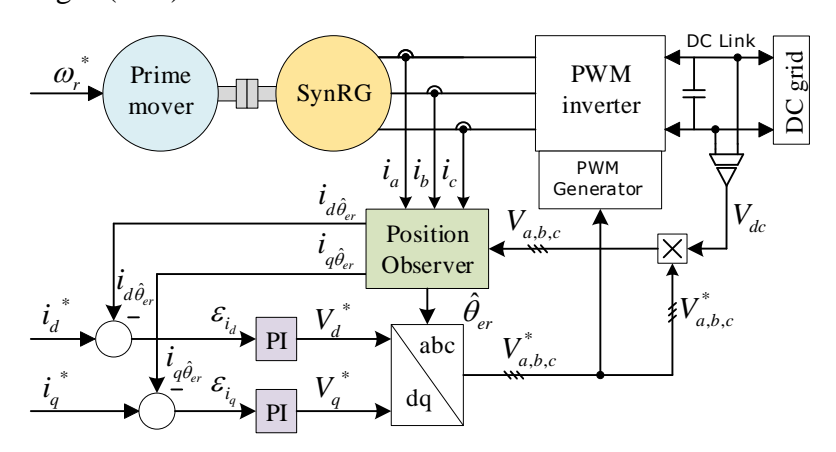


Fig. 2 Sensorless control strategy diagram of the SynRG

A control methodology implemented in a dq-axis reference frame requires knowing the rotor position, mainly for coordinate transformation and parameter measurements. The real SynRG rotating dq-axis reference frame (dq) differs from the stationary $\alpha\beta$ – reference frame with the rotor position θ_{er} , and has the angular speed ω_{er} . When an encoder is used to provide the actual rotor position θ_{er} , the control technique is aligned with the real dq-axis reference frame. In contrast, sensorless control drives the SynRG without an encoder, so the rotor position must be estimated. This leads to an estimated dq-axis reference frame ($\hat{d}\hat{q}$) with an estimated rotor position ($\hat{\theta}_{er}$) relative to $\alpha\beta$ – reference frame. The $\hat{d}\hat{q}$ frame rotates with the estimated angular speed $\hat{\omega}_{er}$



and has an error position ε_{θ} compared to the real dq-axis reference frame. The purpose of a position observer is to find the position error, and so to align the estimated $\hat{d}\hat{q}$ frame with the real one. The overall performance of the control methodology depends on the accuracy of the rotor position estimation. The here proposed rotor position observer model is based on the same dq-axis model of the SynRG, which has the estimated dq-axis reference frame $(\hat{d}\hat{q})$. To estimate the rotor position $\hat{\theta}_{er}$, the observer's estimated q-axis current $(\hat{\iota}_q)$ is compared with the measured q-axis current $(\hat{\iota}_{q\hat{\theta}_{er}})$ transformed into rotor coordinates using $\hat{\theta}_{er}$. The resulted q-axis currents error $(\varepsilon_{\hat{\iota}_{d\hat{\theta}_{er}}})$ is processed by a PI controller whose output represents the estimated speed $(\hat{\omega}_{er})$. Basically the $\hat{\theta}_{er}$ is adjusted until the q-axis currents error is zero, which means that measured q-axis current is equal to the estimated one and so obtaining the real rotor position. For this case, the PI controller and the coordinate transformations form a behavior similar to a phase-locked loop (PLL).

An analysis was conducted to understand better how the differences between the values of the dq-axis inductances and stator resistance introduced into the observer compared to actual values of the SynRG influence the position error. To accomplish this, the position error (ε_{θ}) was expressed considering both the SynRG and observer models. This led to a steady-state equation that was solved using Matlab software. Based on the equation solution, simulations were performed at different dq-axis current references and speed values and for variation of the stator resistance and inductances in p.u. between 0.5 and 2.

The above steady-state analysis revealed how the estimated SynRG rotor position, by the observer, is affected by the differences between the stator phase resistance and dq-axis inductances set in the observer and their actual values in the SynRG. However, this analysis does not establish whether the steady-state solution is stable or how the PI controller coefficients of the observer affect the stability. Therefore, a stability analysis was performed through linearization based on small deviations in the state variables around a steady-state point. After obtaining the linearized system of equations, the Routh-Hurwitz Criterion was used to analyze the stability of the observer for each combination of speed (60, 120, and 200rpm), of different pairs of dq-axis current references, of the parameters k_r , k_d , k_q (within the range of 0.5 to 2 using a step of 0.1) and of the PI controller coefficients k_p and k_i (values were considered from 1 to 10^6 , logarithmically distributed). From all results, a feasibility range for the PI controller coefficients that are most plausible to ensure the stability of the observer was obtained by evaluating the Hurwitz Criterion of $2x10^9$ times and performing intersections of $2x10^5$ feasibility matrices (Fig. 3). Algorithms were developed in Matlab software for solving the position error sensitivity equation, conducting position error analysis, and investigating observer stability (available in thesis appendices 1-3).

The control strategy was first validated through simulations and then by the experimental results while operating the SynRG at rated values and between them. Also, this is supported by extensive simulation and experimental work for operating the SynRG starting from 60rpm up to 200rpm with required torque reference to produce output power from zero up to full load (about 200Nm). Operating at a lower speed than 60rpm could not be achieved due to the voltage drop across the stator resistance (R_s =6.17 Ω). The experimental results show that the torque and speed estimated by the observer closely match those estimated by the IM's inverter, even when SynRG operates with overmodulated voltages. Torque pulsation can also be observed, with an amplitude variation of about $\pm 1\%$ related to the average value, when the phase voltages are saturated (due to insufficient DC-Link voltage).



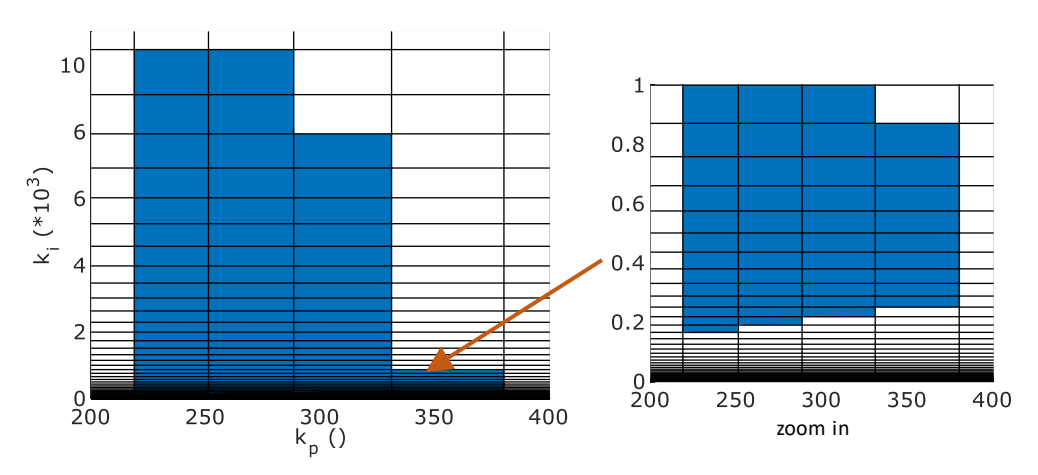


Fig. 3 Feasibility range for kp and ki (left); close-up (right); multiple idq pairs

At this stage, the required output power from the SynRG was set by manually prescribing the dq-axis current references. This approach was done to analyze the observer's behavior and to verify the stability analysis without the influence of an additional PI controller.

A more in-depth analysis proves that the system remains stable for variations in the perunit observer parameters within the following ranges: k_r =-15% to +25%; k_d = ±25%; k_q = -10% to 20% (Fig. 4). Higher variation may be accepted depending on the operating conditions. However, if the observer's dq-axis inductances are set with a ratio higher than the saliency ratio of the SynRG (L_d/L_q =2.7 for this prototype), the control strategy becomes unstable. The method presented for analyzing the position error and stability could also be used to evaluate the performances of the rotor position observer from the literature, such as those related to stator flux position angle [6], [7], [8], or active flux position angle [9].

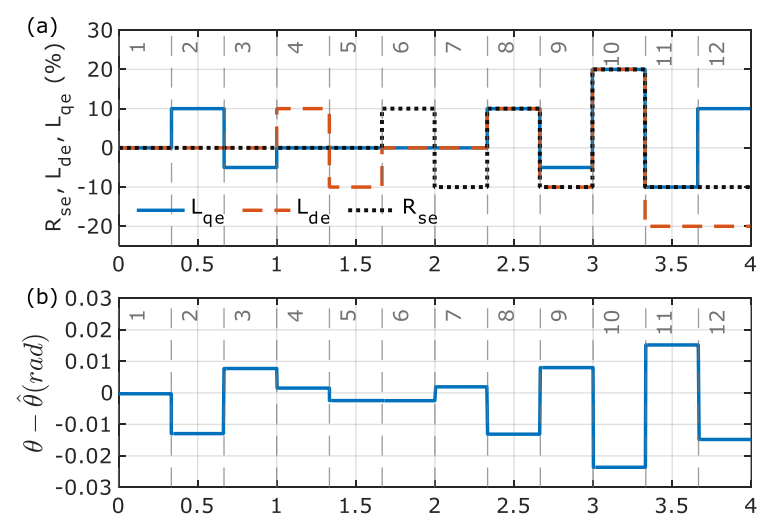


Fig. 4 Observer estimated values according to variation of the uncertain parameters: (a) Variation in the percentage of the R_{se} , L_{de} , L_{qe} related to the SynRG parameters, (b) the difference between the actual and estimated rotor position

The overall results show that the proposed control strategy operates well, also confirming the stability analysis. This control method could represent an alternative to the existing sensorless control strategy of the SynRG to avoid initial flux value compensation, integrators offset, and the



need for a DC voltage buffer in the signal injection method. Improved stability and energy efficiency results can be obtained for a higher saliency ratio (L_d/L_a) of the SynRG.

The speed ranges of the SynRG are suitable for wind and hydro turbine applications. As an extended work to this chapter, the author developed a low-cost hardware-in-the-loop wind turbine emulator to serve as a Prime Mover for SynRG. The emulator was already successfully tested on a low-speed (120rpm), 5kVA permanent magnet synchronous generator (PMSG), as detailed in [10].

Chapter 3 presents an in-depth analysis of the parameters and performances of a 10kW (40Nm, 2.4-4.8krpm) Axially Laminated Anisotropic Rotor Synchronous Reluctance Machine (ALA Rotor RSM) manufactured prototype and proposes a control strategy that aims to operate the machine at the maximum efficiency points.

The lab-scale ALA Rotor RSM prototype (Fig. 5) was designed and manufactured for traction applications to investigate whether this could be a more efficient alternative to the widespread conventional IMs and a cost-effective solution compared with PM machines, assuming the performance concessions associated with the latter one [11]. The prototype has four poles, a rated power of 10kW, a rated torque of 40Nm at the based speed of 2400rpm, and a torque of 20Nm at the maximum speed of 4800 rpm, meaning a constant power speed range (CPSR) of 2 to 1. To allow further investigations regarding the possibility of extending the constant power speed range (CPSR) and to be more phase fault-tolerant, the stator is designed with two twin three-phase windings of double-layer type, each having eight diametrical coils per phase and nine turns per coil. To reduce the rotor iron losses and the torque pulsations, this was divided into three segments with a skewing of 7.5mm (15 electrical degrees) between each other. Each segment has a length of 45mm, resulting in a total rotor stack length of 135mm and a total skewing of 15mm, corresponding to one stator slot pitch.







Final prototype Fig. 5 The manufactured ALA Rotor Lab Prototype (10kW)

After designing and manufacturing an electrical machine prototype, an important step is to validate through experimental measurements the assumptions from the earlier design stage, which are also required for designing and implementing the control strategy [12]. The parameters were measured using both DC and AC standstill tests to determine the dq-axis inductances, including the cross-coupling effect only for the d-axis (Fig. 6). The q-axis inductance with cross-coupling effect could not be measured because the flux linkages $\Psi_{b,c}$ could not be equated with half of the Ψ_{a} . The q-axis inductance determined through DC current decay test is presented in Fig. 7.



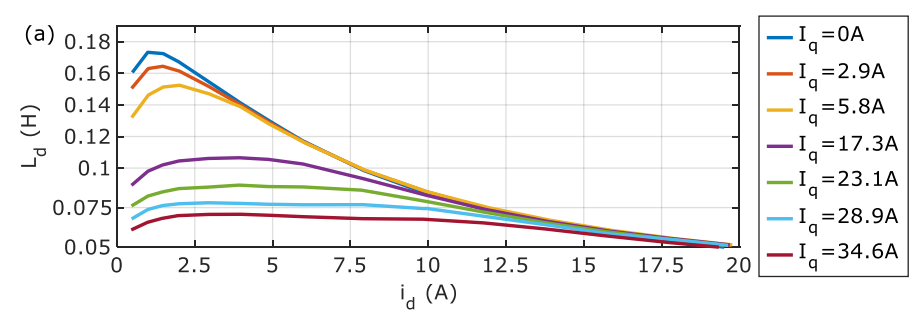


Fig. 6 Decay current experiments with cross-coupling effect: d-axis inductance characteristics (L_d)

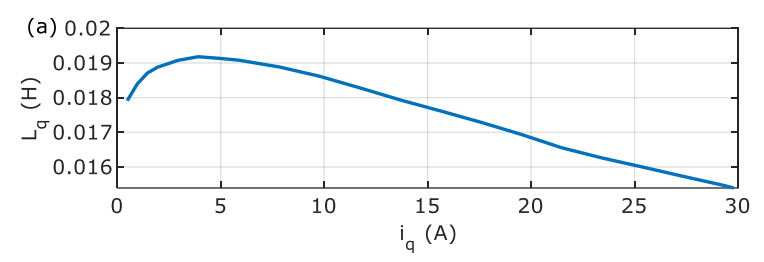


Fig. 7 Decay current experiments without cross-coupling effect: q-axis inductance (Lq)

AC standstill experimental tests were performed to analyze how the frequency influences the dq-axis inductance characteristics due to iron losses and to compare the results with those obtained through the current decay method. The obtained dq-axis inductances at a 5Hz frequency are slightly higher than those resulting from the DC-current decay method. This is somewhat to be expected as the current decay method is more prone to error measurements due to the probe offsets, even though they were compensated, and due to the possible remanent flux density into the laminations after the ending of the decay period. One drawback of this method is the challenges of processing the AC-measured voltage and current and, particularly, in the accuracy of establishing the zero-crossing point, which is crucial to having a consistent angle (ϕ) value determination between the voltage and current over all the acquired signal periods. This issue can lead to errors in the determination of the dq-axis inductance values of up to 20%. A method to increase the accuracy of detecting the zero-crossing point was proposed, and a ready-to-use algorithm was developed to apply it (Available in thesis Appendix 5).

Running tests were performed without an inverter (capacitor self-excited) to explore the iron losses and prototype capabilities of producing the rated torque. An induction machine (IM), driven by an ABB inverter with DTC control, was used as a prime mover to operate the prototype in generator mode at various running speeds. Considering that the ALA Rotor RSM is a PM-less machine, capacitors in a three-phase delta configuration (C_{Δ}) were used for self-excitation with different capacitance configurations to maintain the induced voltage within the boundary limits according to running speeds and load values. To test the prototype at different power levels, a three-phase configurable resistive load (R_{load}) was used to dissipate the generated power. The input mechanical power (p_{input}) was measured using a $\pm 50 Nm$ torque transducer and an encoder, while an oscilloscope was used to measure the output electrical power (p_{el}). To separate the iron losses initially, the mechanical losses were experimentally measured by driving the prototype, without any excitation current, by the IM within the speed range from 100rpm up to 4800rpm with an increment of 100rpm. The copper losses were determined by measuring the stator resistance (Rs)



for each performed test using an LCR meter set in DC mode. A sample of the results is presented in Fig. 8.

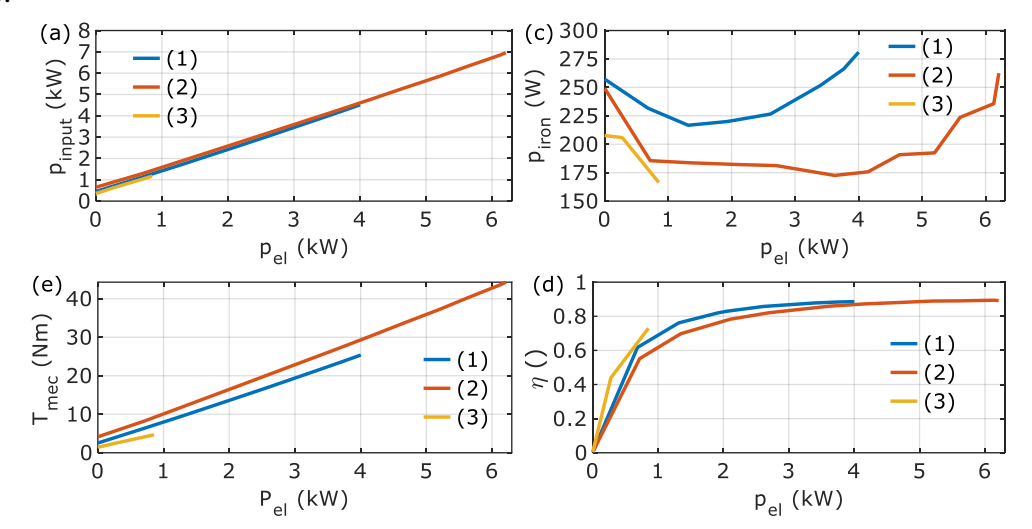


Fig. 8 ALA Rotor RSM Capacitors Self-Excited, iron loss investigation under resistive load conditions - experimental results: (1) c=33.4μF, n=1700rpm; (2) c=66μF, n=1500rpm; (3) c=25μF, n=2400rpm;

To process the high amount of measured data, ready-to-use algorithms were developed for multiple file processing, for accurately detecting the zero-crossing of the AC waves, and for the evaluation of the measurements to provide the inductances, RMS value for phase voltages and currents, losses, torque, speed, linkage flux, induced voltage, and efficiency (available in thesis appendices 4-6).

Further, this chapter analyses the performances of the ALA Rotor RSM and its driver inverter for a high range of operating speed and torque values using a dq-rotor frame control strategy. The experimental platform used for this tests is presented in Fig. 9.

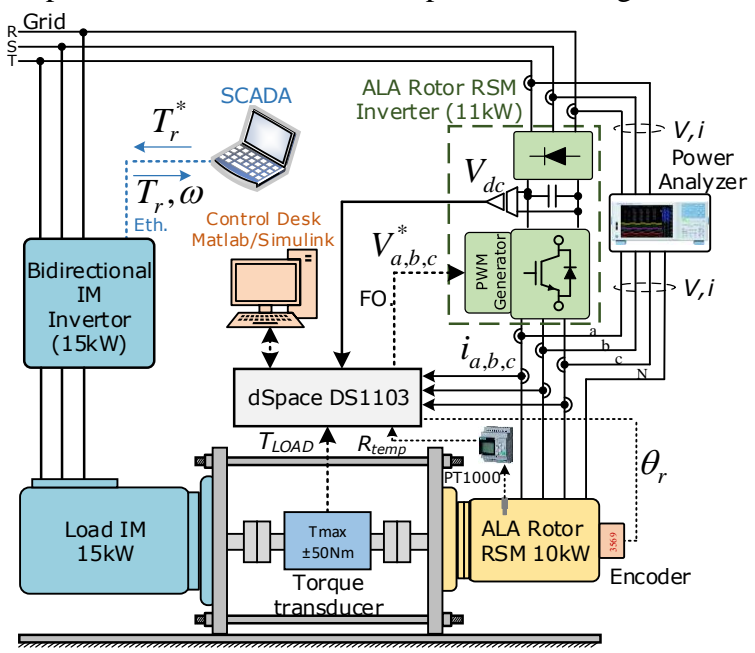


Fig. 9 Performances assessment of the ALA Rotor RSM - Experimental setup diagram



Various dq-axis reference currents were prescribed within the boundaries of stability limits for each running speed and torque value in an effort to find the dq-axis pair that will produce the maximum efficiency. The efficiency of both the ALA Rotor RSM and its inverter was determined by using a power analyzer to measure the input and output electrical power of the inverter, while the mechanical output power of the ALA Rotor RSM was calculated using the torque and speed values provided by the torque transducer and encoder, respectively.

From all measurements, the points that provide the maximum efficiency of both the ALA Rotor RSM (Fig. 10) and its drive inverter were extracted based on which the dq-axis current characteristics were generated. Additionally, for each operating point, the input active and apparent power for both the inverter and ALA Rotor RSM, the total and the fundamental power factor, and the iron and copper losses for the ALA Rotor RSM were measured. These provided a deep understanding of the ALA Rotor RSM behavior and how the prescribed dq-axis current pairs influence the performances.

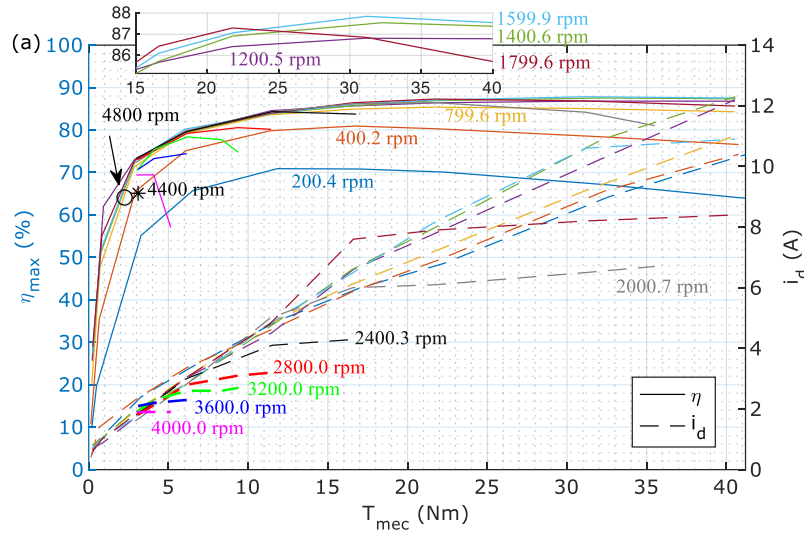


Fig. 10 Measured maximum efficiency characteristics of the ALA Rotor RSM

Forwards, a simulation model for the ALA Rotor RSM is presented, which includes the dq-axis measured inductances with cross-coupling and the measured mechanical, copper, and iron losses. Considering the complexity of using the directly measured values, methods of approximating these are shown. Additionally, for the inductances case, the approximation function based on the reciprocity theorem determines the q-axis inductance with cross-coupling effect using the cross-coupling measurements performed for the d-axis one. These ensure a correlation between the manufactured prototype and the simulation model as close as possible.

Following this, the proposed control strategy for the ALA Rotor RSM is presented. This is based on a Maximum Torque per Amper (MTPA) offline computed function (OFC) with a smooth transition to a Maximum Torque per Flux (MTPF) function for the saturated sections. The diagram of the proposed method is shown in Fig. 11. A PI speed controller is used to prescribe the required q-axis current, which is compared with the maximum achievable current within the limits of available magnetic flux, and the lower value between them is prescribed as a reference q-axis current. The d-axis current reference is obtained either from the MTPA function based on the input q-axis reference or from the MTPF function according to the operating conditions. Then, both dq-



axis current references are compared with the measured ones, and the resulting errors are processed by PI controllers whose outputs represent the dq-axis voltage references for the drive inverter.

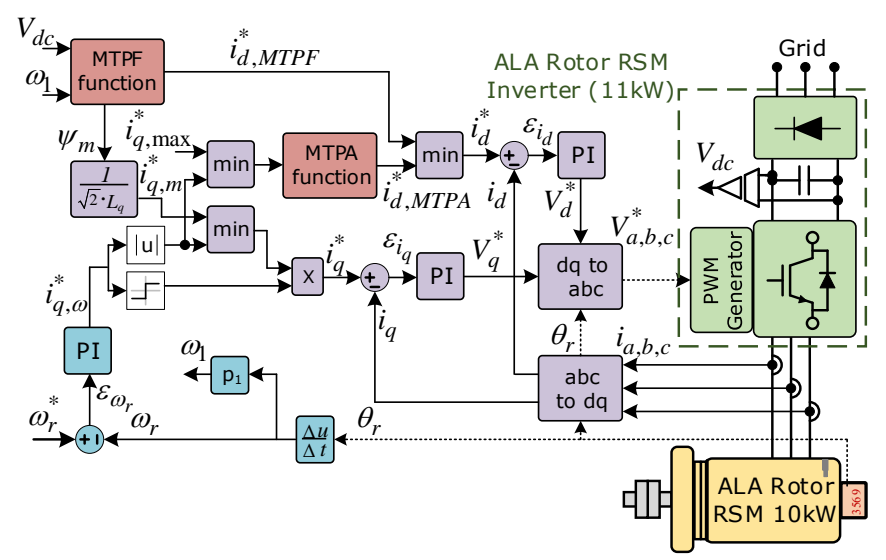


Fig. 11 ALA Rotor RSM Proposed control strategy diagram

The proposed method for the MTPA is to use an algorithm (available in Appendix 8 of the thesis) that computes the optimal dq-axis current dependency offline using only the measured dq-axis inductances (with cross-coupling effect) prior to the commissioning of the ALA Rotor RSM. Essentially, the algorithm generates an electromagnetic torque matrix for various combinations of dq-axis currents (four million for this ALA Rotor RSM). From this matrix, the dq-axis current pairs that yield the highest torque values are selected, and the dependency of the d-axis current on the q-axis current is obtained, as illustrated in Fig. 12 (blue line). To simplify the implementation, this was fitted with a first-order polynomial function (red line), which represents the MTPA function $(i_{d,MTPA}^* = d_1 \cdot i_a^* + d_0)$.

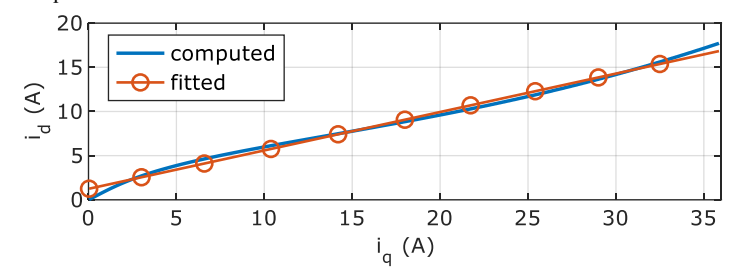


Fig. 12 Computed vs. fitted MTPA function $i_d=f(i_q)$

The MTPF function provides the dq-axis currents within the maximum available magnetic flux. This is determined based on the actual running speed, actual DC-Link voltage, and the d-axis inductance with cross-coupling effect. The d-axis inductance is implemented as an approximated function from those measured through DC current decay, considering the most probable operating sections of the ALA Rotor RSM with MTPF.

To evaluate the proposed control strategy, a look-up table function based on the measured dq-axis current characteristics that provided the maximum efficiency was developed (MLT) to cover the entire speed range, as the measurements were only acquired at several speed values. The



results are presented in Fig. 13 compared with the measured dq-axis current pairs. As observed, this fits almost perfectly the measured curves.

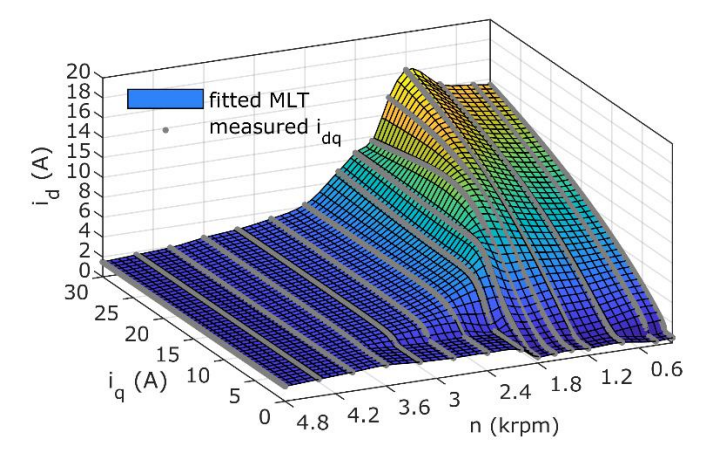
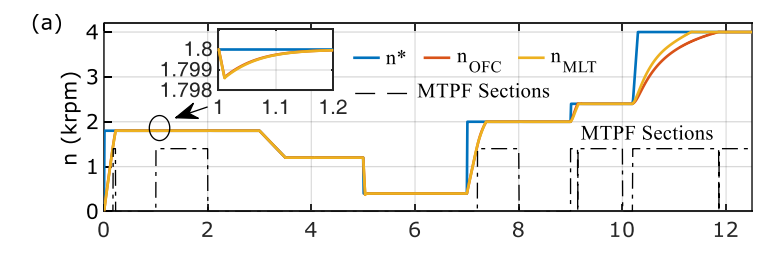


Fig. 13 MLT function fitted look-up table vs. measured dq-axis current pairs

Before being used as a validation method, the MLT was verified by performing simulations and comparing the results with those obtained from the experimental measurements, which were approximately the same. This also validates the ALA Rotor RSM simulation model and the goodness of the approximation functions for the dq-axis inductances, copper, mechanical, and iron losses. The here-generated look-up table function (MLT) based on the measured dq-axis current pairs that drive the ALA Rotor RSM to its maximum efficiency can be used as a control method. This definitely will provide the optimum dq-axis current pairs being previously measured. However, the major drawback lies in the large amount of experimental measurements required to provide sufficient data to identify the maximum efficiency point for creating the look-up table.

Finally, the proposed control strategy (OFC) is compared with the MLT through simulations. A sample is presented in Fig. 14 for operating at various speed and torque values. The chart (h) shows the efficiency achieved by the ALA Rotor RSM using both methods. The results indicate that this method is a promising alternative for driving the ALA Rotor RSM closely to its maximum efficiency over a wide range of speeds and loading torques, even when the machine is highly saturated. The transition between the MTPA and MTPF is seamless in both directions without causing any perturbations.





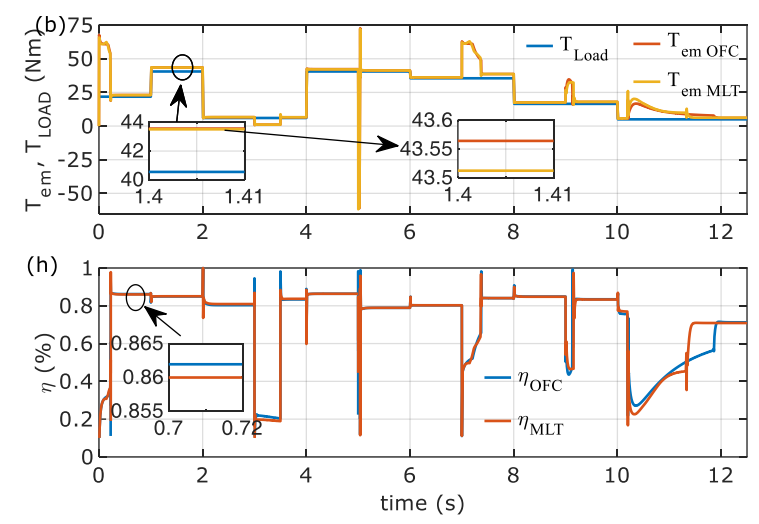


Fig. 14 ALA Rotor RSM Simulation Results OFC vs. MLT: (a) reference vs. actual speed; (b) loading vs. electromagnetic torque; (h) OFC vs. MLT efficiency

A drawback of the method is the initial required measured dq-axis inductances with at least cross-coupling effect for the d-axis. However, this is compensated by the method's main advantage, which relies on the ease of implementation, considering that the resulting MTPA function is a first-order degree equation, which is also less susceptible to stability issues. Additionally, for traction applications (and not only) where the ALA Rotor RSM may be mass-produced, the initial experimental measurements are performed a single time. Even more, the experimental procedure can be automated and completed within one or two hours.

Chapter 4 presents a proposed concept for a fully electric city minibus for public transportation using supercapacitors (SC) as storage elements [13], [14]. A usually commercial internal combustion engine (IEC) minibus has been considered and converted by replacing all related equipment for the IEC. The traction is implemented with an interior permanent magnet synchronous motor (IPMSM) which has Bonded-NdFeB Spoke PMs placed on axis d, and flux barriers on axis q driven by an inverter with vector control strategy. A high-ratio bidirectional hybrid DC-DC converter (HBDC) ensures the power transfer between the SC, inverter DC link, and charging power line. The system is studied for two cases: (i) full scale 7t minibus for which simulation results are provided for various operating conditions (road slope, wind speed, load, etc.) and for a case study with a measured real driving cycle profile; (ii) 1:20 laboratory scale where an emulator experimental platform has been developed including the IPMSM, SC, and HBDC.

The city minibus concept has been proposed, developed, implemented, and analyzed through an experimental demonstrative project (PED) founded by the Romanian Ministry of Research and Innovation [15]. The block diagram of the minibus energy conversion, storage, and propulsion system (ECSPS) is presented in Fig. 15. As can be observed, the primary ECSPS storage consists of supercapacitors connected to a common DC link through a bidirectional DC-DC converter, named together converter-supercapacitor unit (CSU). The storage is modular, and the number of the CSU units is established depending on the minibus's required range and design limitations. As a backup solution, an auxiliary small battery module (BM) provides energy to the DC link to cover a short distance in case of empty CSUs. The electric traction motor is a high-



density torque IPMSM driven by a bidirectional inverter with vector control. The IPMSM is directly coupled, without a gearbox, to the transmission due to the motor's high starting torque. Also, an encoder provides the rotor position to calculate stator flux and reference phase voltages. The control of the power transfer and DC link voltage level is assured by the energy management system (EMS). Considering the limitations given by the available equipment in the laboratory, the further analyzed structure has been simplified regarding storage, having only one CSU and without BM. The simplified block diagram resembles a battery-electric vehicle (BEV) where the SC replaced the battery pack. The HBDC transfers the power from the SC to the DC link and viceversa during the regenerative braking period or when it charges from stations. The HBDC has a high voltage conversion ratio due to the voltage variation of the SC.

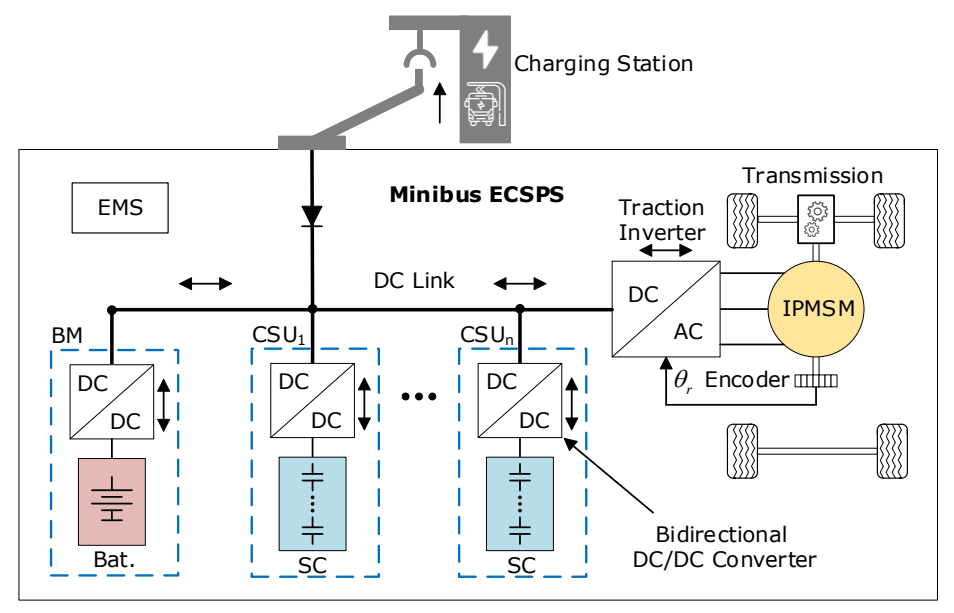


Fig. 15 City minibus concept – block diagram

The first part of the chapter shows the mathematical models for each component and compares the main components' weights between the usual minibus with IEC and the minibus equipped with electric traction. Following this, the proposed drive control methodology was explained, and simulations for the full-scale case were performed for a synthetic speed profile, considering normal operation and operation in case of power converter failure. The designed bonded-NdFeB IPMSM for the full-scale case has six poles (separate laminated), 100kW rated power, and 400Nm nominal torque at 2400rpm base speed. The rotor has two segments shifted with 30 electrical degrees to reduce the torque ripple and flux rotor barriers for a lower q-axis inductance. The IPMSM design aspects also included a 2 to 1 constant power speed range for a given DC-Link inverter voltage. More details about the design aspects and FEM validation results are given in [16]. The SC module has been designed to have a storage capacity of approximately 8.52kWh. The value was determined considering the minibus energy consumption at full load (7t) for a driving route with a length of 6.2km, five bus stations, a road slope of 10% for 200m length, several travel speeds (30, 50 and 70 km/h), and a value of 17.1m/s wind speed. From the total available power of the SC, only 75% is used due to the SC's natural voltage characteristic, which will lead to high currents through SC and HBDC, thus reducing their efficiency. Discharging the



SC more than 25% will also require a higher voltage ratio for the HBDC. In the design, a time limit of one minute (usually required time for a bus stop) was also taken into account for the complete charging of the SC from the 25% state of charge and an additional 2.5kWh of energy consumption by the auxiliary equipment of the minibus.

Then, simulations were performed on a measured driving cycle profile with real traffic conditions to verify and validate the proposed minibus concept and the drive control methodology. The driving cycle profile has been acquired for a bus line (Bus line 16) from Timisoara (Romania) operated by a trolleybus (Fig. 17). The bus line has seven intermediate bus stations, a total length of 4.26km, and the road steep is close to 0% (the Timisoara city is located in the Western Romania Plain).



Fig. 16 Bus line 16 Timisoara, Romania (Google Maps 2021) and measured trolleybus speed

A sample of the simulation results are presented in Fig. 17. As can be observed in Fig. 17 – chart (a)., sections with steep acceleration (ex. 600s timestamp) show a slight difference between the actual and reference power train speed, caused perhaps by the high torque developed by trolleybus's ICE at the transmission due to existing of the gearbox or by some measurement errors.

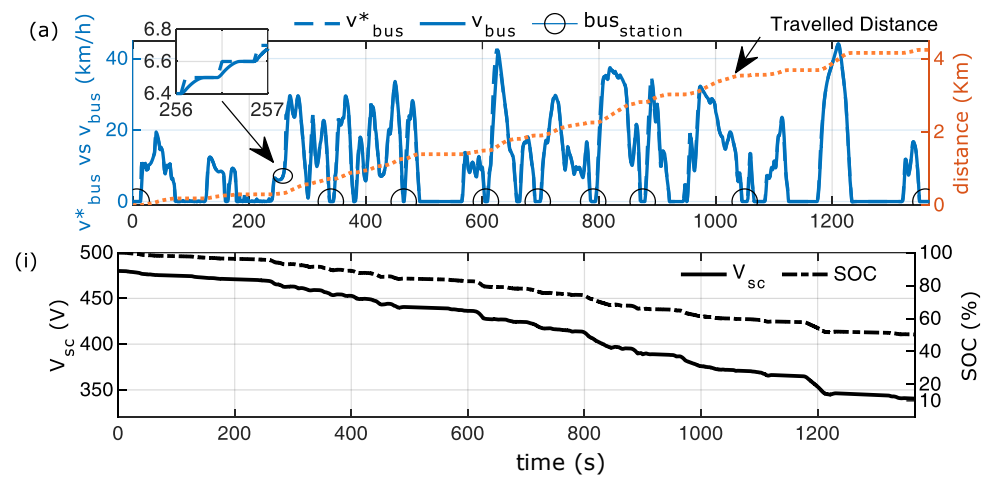


Fig. 17 Real traffic conditions operation: (a) Minibus velocity (reference vs. actual) and traveled distance; (i) SC module voltage and state of charge (SOC);



The IPMSM can produce the required torque to achieve the reference speed (given the short period), but the current through the traction inverter is limited. It is not feasible for urban public transportation to design the traction inverter for higher power than 140% of the rated motor power only to achieve higher acceleration, considering that moderate accelerations are recommended.

The results prove the minibus concept and show that the IPMSM is operating well. It also reveals that the SC storage and the power converters have to be designed according to utilization location and route length (when possible) to achieve the highest passenger load factor. For the studied route, during normal operation, the SC can be charged within 8 minutes at the end of the route using an already existing charging station. This can be compared with an operation similar to that of an IEC minibus, which has a brief brake at the end of the route. Based on the simulation results provided by the case study, a cost comparison between the LiB and the SC storage shows significant financial advantages (~2 to 1) of using SC as storage for this particular application, considering their entire operational lifespan.

The second part of the chapter presented simulation and experimental results for the lab scale (1:20). To validate the proposed power train and the drive control methodology, a 1:20 scale 5kW (2.4-4.8krpm, 20-10Nm) IPMSM laboratory prototype has been designed and manufactured (Fig. 18) based on the full-scale (1:1) IPMSM design. Initial standstill tests were performed to determine the dq-axis inductances, followed by the generator tests to verify the design parameters. A dedicated platform was built to test the operation of the IPMSM for steady-state and transient regimes. The experimental results proved the operation of the IPMSM over the entire speed range characteristics and its capabilities to produce 20Nm at 2400rpm and 10Nm at 4800rpm. Additionally, a modified supertwisting sliding mode speed controller was proposed for the control strategy to enhance the q-axis references for the PI current controller.



Fig. 18 The manufactured IPMSM Lab Prototype (5kW)

Finally, to validate the proposed minibus power system concept, an experimental platform, including the SC and HBDC components, has been developed (Fig. 20-Fig. 21). The platform is based on the proposed concept described above. The HBDC converter transfers the power bidirectionally to and from the SC to maintain the IPMSM drive inverter DC-Link level at 375V (set for safety reasons). The DC-Link rated voltage level has been set at 375V for safety reasons. The HBDC maintains the voltage level by discharging the SC while the IPMSM drives the transmission and by charging the SC during the regenerative braking of the IPMSM. To simulate the charging of the SC while the minibus is stopped at the charging stations, a DC source is used, connected to the DC-Link bus through a diode to prevent reverse power flow. For emulating the



transmission resistive torque, a 15kW squirrel cage induction motor (IM) is used coupled with the IPMSM through a torque transducer with ±100Nm torque range measurement. A 15kW industrial bidirectional DTC power converter drives the asynchronous machine with torque reference computed based on the transmission mathematical model. The algorithm is implemented on an industrial programmable logic controller (PLC) for real-time calculations. The HBDC converter is a prototype developed for this project [17]. It is a hybrid bidirectional switched capacitor DC-DC converter (BHCC) with a wide ratio voltage suitable for the variation of the SC output voltage. This is an improved topology, which, in addition to the conventional topologies, besides the high ratio conversion voltage, has advantages such as smaller passive components and lower active device stress.

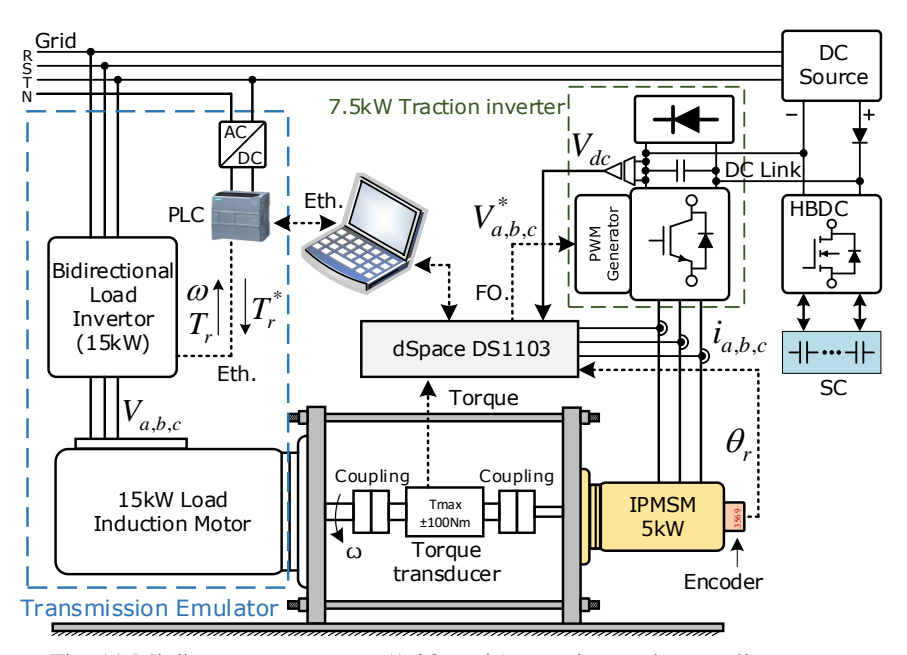


Fig. 19 Minibus power system (1:20 scale) experimental setup diagram

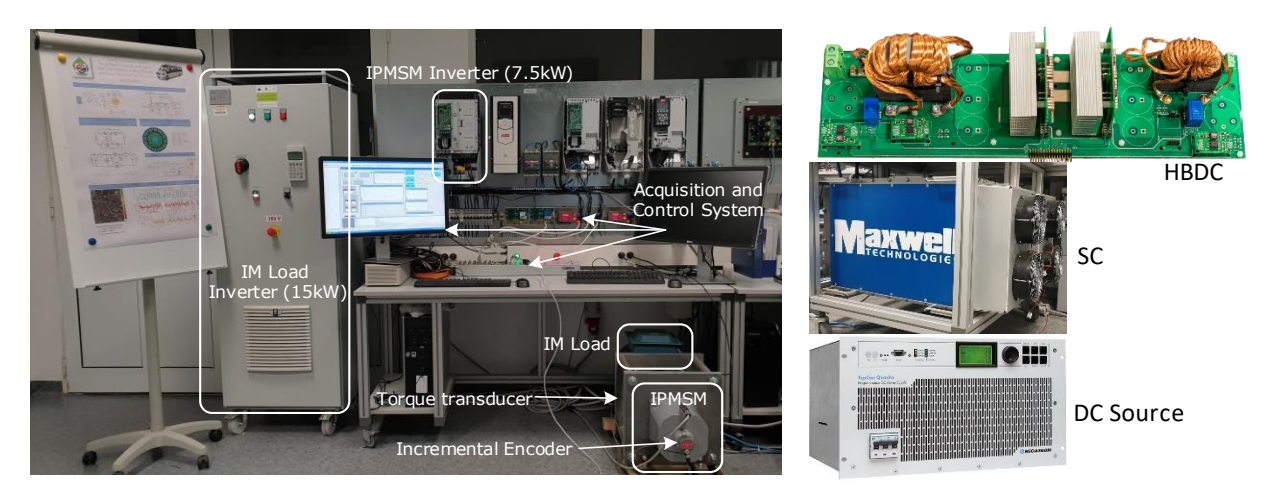


Fig. 20 Minibus power system (1:20 scale) experimental platform

Extensive experimental investigations were done with all components of the minibus power system, focusing on both steady-state and transient minibus operation. A sample of the



experimental results is shown in Fig. 21. The obtained results show an overall good operation of the entire system, confirming the initial simulations. It can be assumed that the full-scale minibus would have similar performance.

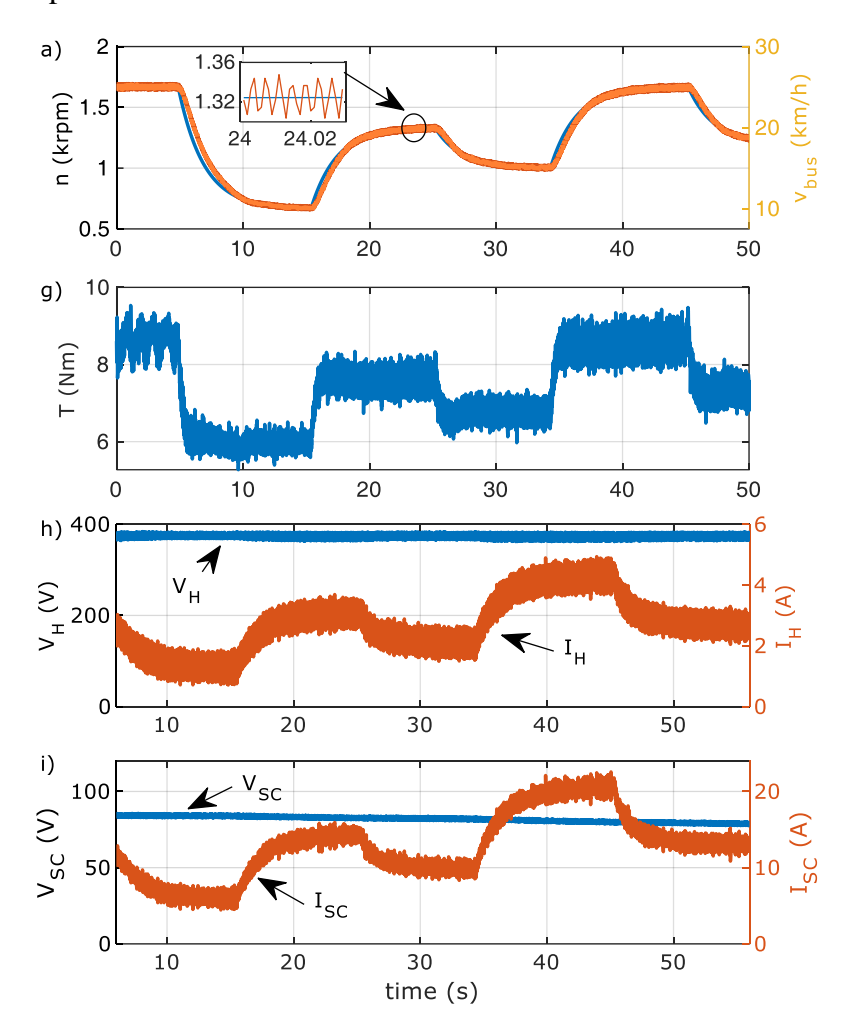


Fig. 21 a) Reference vs. measured angular speed (left axis), minibus speed in km/h (right axis); g) IPMSM loading torque; h) BHCC High-side voltage and current, i) BHCC SC-side voltage and current

Chapter 5 presents the conclusions of the thesis, the original contribution of the author, and future work for the presented subjects.

This thesis focuses on control strategies for PM and reluctance electric motors, analyses their performances, and explores their potential for renewable energy conversion and automotive applications. Four control strategies were proposed: one is a sensorless method dedicated to SynRG for renewable applications, while the other three use an encoder to provide the rotor position and are dedicated to IPMSM and ALA Rotor RSM for traction applications. The IPMSM and ALA Rotor RSM are two newly designed and manufactured prototypes analyzed in this thesis through extensive experimental characterizations and by operating in various conditions within the specified applications using the proposed control strategies. These two motors were investigated in an effort to provide improved electric machines with lower costs and better performances over



a wide speed range. Research has proved for the IPMSM that using Bonded NdFeB PMs can be a cost-effective alternative to Sintered NdFeB PMs [18] and also its capabilities of achieving a constant power speed range (CPSR) of 2 to 1. The ALA Rotor RSM prototype, studied in detail, achieved an efficiency of ~90% in generator mode and ~88% in motor mode and a saliency ratio that varies from ~9 to ~4.5 according to operating conditions. Regarding efficiency, it is considered that a higher value can be obtained by connecting the two stator windings in parallel, thus extending the speed range at rated torque for which the ALA Rotor RSM does not saturate. It is anticipated that a CPSR of 2 to 1 can be obtained within the designed speed range.

For the sensorless control method, a stability analysis was performed, which aims to provide a feasibility range for the PI controller coefficients for which the observer is stable with respect to the limits of the parameter differences between the observer and SynRG. Coefficients from the feasibility range were selected, and the results obtained through simulation and experimental tests validated the stable operation of the observer. Also, a position error analysis was performed to reveal how the estimated rotor position is affected by the uncertainties of the machine parameters. A more in-depth analysis proves that the system remains stable for variations in the per-unit observer parameters within the following ranges: k_r =-15% to +25%; k_d = ±25%; k_q = -10% to 20%. Higher variation may be accepted depending on the operating conditions. The method presented for analyzing the position error, and stability could also be used to evaluate the performances of the rotor position observer from the literature, such as those related to stator flux position angle or active flux position angle [11].

The proposed control strategy for the ALA Rotor RSM is a promising alternative for driving the ALA Rotor RSM closely to its maximum efficiency over a wide range of speeds and loading torques, even when the machine is highly saturated. A drawback of the method is the initial required measured dq-axis inductances with at least cross-coupling effect for the d-axis. However, this is compensated by the method's main advantage, which relies on the ease of implementation, considering that the resulting MTPA function is a first-order degree equation, which is also less susceptible to stability issues. Used to validate the proposed control strategy, the measured look-up table control method (MLT) can also represent an alternative control strategy that will definitely provide the optimum dq-axis current pairs as these were previously measured. The major drawback of the MLT function is the high amount of experimental measurements required to provide sufficient data to identify the maximum efficiency characteristics and thus determine the look-up table function.

The detailed determination of the parameters for the ALA Rotor RSM emphasizes the importance of the methodology used and the accuracy in measuring the quantities of interest. Even if measurements are acquired without errors, their processing can cause errors in the final results of up to 20-30% or even more.

The final part of the thesis proposes a concept for a fully electric city minibus intended for public transportation using supercapacitors as a storage element and a single IPMSM with Bonded-NdFeB Spoke PMs for traction. Two cases are investigated:

- A full-scale model (1:1) for which simulation results in real traffic operating conditions are provided;
- A lab-scale model (1:20) which include a transmission emulator, the IPMSM with its drive inverter, SC, HBDC, and the charging station, for which both simulation and experimental results are presented.



The proposed control strategy for the IPMSM in this application was verified for both the operation of the machine individually and in relation to the other components, including the HBDC and SC. The results obtained for the entire system under real traffic conditions demonstrate that a supercapacitor module (SC) with a capacity of 190F, fully charged (480V), can provide enough energy for a 7-ton minibus, loaded with 28 passengers to cover a distance of 4.2 km on a flat route. However, if there is an altitude variation of 72 meters and an increase in auxiliary energy consumption, an SC module with a capacity of 266F is required, which would reduce the number of passengers to 24. Under normal operating conditions, the minibus can charge the SC module in 8 minutes at the end of the route using a 50 kW electric charging station. If the route is longer, the charging time can be reduced to just one minute, but this would require a 400 kW charging station.

The experimental results obtained for the entire system in laboratory conditions validate the concept and suggest that it can be applied to a real minibus prototype, which is expected to deliver similar performances. The comparative cost analysis between using a lithium-ion battery versus SC as a storage element shows that the SC offers a significant financial advantage, with a ratio of approximately 2.5 to 1 over lithium-ion batteries for this application, considering their entire life span.

Original contribution

The following are the most relevant summarized contributions of the author:

- Analyzing EU Directives, Regulations, and targets for electric motor efficiency and for increasing energy production from renewable sources;
- Performing a survey of the main sensorless control strategies for synchronous reluctance machines;
- Literature review on methods for determining parameters of electrical machines, control strategies with encoder for the ALA Rotor RSM and IMPMSM, and exploring fully electric vehicles that use supercapacitor as storage element;
- Proposing a sensorless control strategy for the low-speed synchronous reluctance generator based on the q-axis estimated current. Performing of a stability analysis for the observer and a position error analysis with SynRG parameters variation;
- Comprehensive experimental parameters determination of the ALA Rotor RSM.
- Experimentally performances assessment of the ALA Rotor RSM and its drive inverter for various combinations of the dq-axis current references within the stability boundaries limits of the machine;
- Introducing into the ALA Rotor RSM model of the saturation, iron, copper, and mechanical losses through different approximation functions;
- Proposing a control strategy based on an offline computed function using the measured dqaxis inductances, which maximizes the efficiency of the ALA Rotor RSM – ready-to-use algorithm, is provided;
- Proposing of a fully electric minibus concept for public transportation using supercapacitors as a storage element and an IPMSM with Bonded-NdFeB Spoke PMs for traction.
- Proposing the drive control strategy for the IPMSM and the modified supertwisting sliding mode controller for the experimental tests.
- Developing the experimental platforms and two SCADA systems for all described applications.



Future work

At least the following paths remain open for further development and improvements:

- The proposed sensorless control method for the SynRG needs improvement, such as a power or voltage controller, and testing the SynRG and the proposed method with the developed hardware-in-the-loop wind turbine emulator (as thesis extension) to analyze the operation under real wind speed profiles;
- Further investigation of the ALA Rotor RSM with the two windings connected in parallel to explore the CPSR of 2 to 1 up to 4800rpm and the variation of the saliency ratio;
- The proposed control method for the ALA Rotor RSM is promising but requires the measurements of the dq-axis inductances with the cross-coupling effect; therefore, a procedure to determine acceptable inductances during the commissioning would enhance the method;
- Although the supercapacitor city minibus concept provided acceptable results on the 1:20 lab scale, and both the proposed control strategy and the Bonded-NdFeB IPMSM showed promising results for the 2 to 1 CPSR operation up to 4800rpm, it should be extended at first for a reduced scale minibus prototype (one or two tones) to facing the challenges related to real operating conditions.

References

- [1] G. Wang, M. Valla, and J. Solsona, "Position Sensorless Permanent Magnet Synchronous Machine Drives—A Review," *IEEE Trans. Ind. Electron.*, vol. 67, no. 7, pp. 5830–5842, Jul. 2020, doi: 10.1109/TIE.2019.2955409.
- [2] "A Review of Synchronous Reluctance Motor-Drive Advancements." Accessed: Mar. 25, 2025. [Online]. Available: https://www.mdpi.com/2071-1050/13/2/729
- [3] A. M. Iuoras, N. C. Szekely, L. D. Vitan, M. Bojan, and P. D. Teodosescu, "AC home appliances retrofiting for DC microgrids," in 2020 12th International Conference on Electronics, Computers and Artificial Intelligence (ECAI), Jun. 2020, pp. 1–6. doi: 10.1109/ECAI50035.2020.9223183.
- [4] R. Buzatu, V. Ungureanu, A. Ciutina, M. Gireadă, D. Vitan, and I. Petran, "Experimental Evaluation of Energy-Efficiency in a Holistically Designed Building," *Energies*, vol. 14, no. 16, Art. no. 16, Jan. 2021, doi: 10.3390/en14165061.
- [5] L.-D. Vitan, L. Tutelea, N. Muntean, and I. Boldea, "Sensorless Synchronous Reluctance Generator Control Based on q Axis Estimated Current," in 2019 International Aegean Conference on Electrical Machines and Power Electronics (ACEMP) & 2019 International Conference on Optimization of Electrical and Electronic Equipment (OPTIM), Aug. 2019, pp. 260–267. doi: 10.1109/ACEMP-OPTIM44294.2019.9007225.
- [6] D. V. M, B. Singh, and B. G, "Position Sensor-less Synchronous Reluctance Generator Based Grid-Tied Wind Energy Conversion System with Adaptive Observer Control," *IEEE Trans. Sustain. Energy*, pp. 1–1, 2019, doi: 10.1109/TSTE.2019.2903891.
- [7] X. Dianguo, J. Xinhai, and C. Wei, "Sensorless control of synchronous reluctance motors," in 2017 IEEE Transportation Electrification Conference and Expo, Asia-Pacific (ITEC Asia-Pacific), Aug. 2017, pp. 1–4. doi: 10.1109/ITEC-AP.2017.8080935.
- [8] I. BOLDEA, Z. X. FU, and S. A. NASAR, "Torque Vector Control (tvc) of Axially-Laminated Anisotropic (ala) Rotor Reluctance Synchronous Motors," *Electr. Mach. Power Syst.*, vol. 19, no. 4, Art. no. 4, Jul. 1991, doi: 10.1080/07313569108909543.
- [9] S. Agarliță, M. Fătu, L. N. Tutelea, F. Blaabjerg, and I. Boldea, "I-f starting and active flux based sensorless vector control of reluctance synchronous motors, with experiments," in 2010 12th International Conference on Optimization of Electrical and Electronic Equipment, May 2010, pp. 337–342. doi: 10.1109/OPTIM.2010.5510564.
- [10] L.-D. Dănuţ, D. Hulea, O. Cornea, N. Muntean, M. A. Iuoras, and N. Hinov, "Low Cost Implementation of a Wind Turbine Emulator," in 2020 IEEE International Conference on Environment and Electrical Engineering and 2020 IEEE Industrial and Commercial Power Systems Europe (EEEIC / I&CPS Europe), Jun. 2020, pp. 1– 6. doi: 10.1109/EEEIC/ICPSEurope49358.2020.9160604.



- [11] I. Boldea, I. Torac, A. Martin, D. Vitan, and L. Tutelea, "Axially-Laminated-Anisotropic-rotor Reluctance Synchronous Motor characterization: analytical design, key FEM validations and preliminary experiments: 10kW, 2.4-4.8krpm," in 2022 IEEE 20th International Power Electronics and Motion Control Conference (PEMC), Sep. 2022, pp. 113–120. doi: 10.1109/PEMC51159.2022.9962869.
- [12] L.-D. Vitan, L. Tutelea, A.-D. Martin, N. Muntean, and I. Boldea, "Axially laminated anisotropic (ALA) rotor reluctance synchronous motor (RSM): comprehensive experiments characterization," in 2023 International Aegean Conference on Electrical Machines and Power Electronics (ACEMP) & 2023 International Conference on Optimization of Electrical and Electronic Equipment (OPTIM), Sep. 2023, pp. 1–6. doi: 10.1109/ACEMP-OPTIM57845.2023.10287071.
- [13] L. D. Vitan, A. Martin, L. Tutelea, I. Boldea, I. Torac, and N. Muntean, "Supercapacitor City Minibus Bonded NdFeB IPMSM Propulsion System: Design and System Modeling Methodology via a Case Study and Laboratory Experiments," *IEEE Trans. Ind. Appl.*, vol. 59, no. 2, pp. 1405–1417, Mar. 2023, doi: 10.1109/TIA.2022.3220500.
- [14] L.-D. Vitan, A.-D. Martin, L. Tutelea, and I. Boldea, "Supercapacitor City Minibus Propulsion System Simulations, Methodology, and Case Study," in 2021 International Aegean Conference on Electrical Machines and Power Electronics (ACEMP) & 2021 International Conference on Optimization of Electrical and Electronic Equipment (OPTIM), Sep. 2021, pp. 181–190. doi: 10.1109/OPTIM-ACEMP50812.2021.9590081.
- [15] "ECOBUS 307PED2020 ECON-BUS 307PED2020." Accessed: Nov. 10, 2024. [Online]. Available: https://www.econbus.academiatm.ro/
- [16] L. Tutelea, I. Torac, and I. Boldea, "100kW 2400-4800rpm -spoke-PM bonded NdFeB traction motor preliminary design with FEM imported parameter circuit controlled dynamics validation," in 2021 International Aegean Conference on Electrical Machines and Power Electronics (ACEMP) & 2021 International Conference on Optimization of Electrical and Electronic Equipment (OPTIM), Sep. 2021, pp. 72–78. doi: 10.1109/OPTIM-ACEMP50812.2021.9590050.
- [17] D. Hulea, M. Gireadă, O. Cornea, and N. Muntean, "An Improved Bidirectional Hybrid Switched Capacitor Converter," in *IECON* 2022 48th Annual Conference of the *IEEE Industrial Electronics Society*, Oct. 2022, pp. 1–6. doi: 10.1109/IECON49645.2022.9969058.
- [18] D. D. Patel, I. Boldea, and B. Fahimi, "Bonded Nd-PM Claw-Pole Synchronous Motor Drive for Traction Applications: Benefits and Challenges," in 2023 IEEE Energy Conversion Congress and Exposition (ECCE), Oct. 2023, pp. 4682–4689. doi: 10.1109/ECCE53617.2023.10362865.